

Interaction-Dependent Interfacial Charge-Transfer Behavior in Solar Water-Splitting Systems

Guancai Xie,^{†,‡,||} Liming Guan,^{†,||} Linjuan Zhang,^{§,||} Beidou Guo,^{†,‡} Aisha Batool,^{†,‡} Qi Xin,[†] Rajender Boddula,^{†,‡} Saad Ullah Jan,^{†,‡} and Jian Ru Gong^{*,†,||}

[†]Chinese Academy of Sciences (CAS) Key Laboratory for Nanosystem and Hierarchical Fabrication, CAS Center for Excellence in Nanoscience, National Center for Nanoscience and Technology, Beijing 100190, PR China

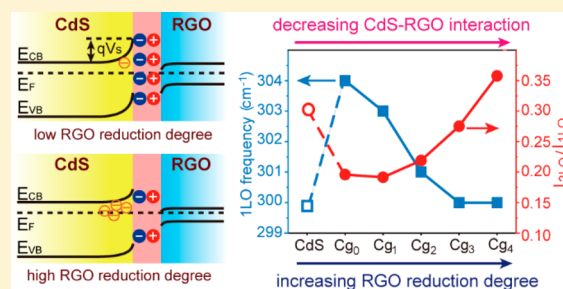
[‡]University of Chinese Academy of Sciences, Beijing 100049, PR China

[§]Shanghai Institute of Applied Physics, Chinese Academy of Science, Shanghai 201800, PR China

S Supporting Information

ABSTRACT: Dual-band-gap systems are promising for solar water splitting due to their excellent light-harvesting capability and high charge-separation efficiency. However, a fundamental understanding of interfacial charge-transfer behavior in the dual-band-gap configuration is still incomplete. Taking CdS/reduced graphene oxide (CdS/RGO) nanoheterojunctions as a model solar water splitting system, we attempt here to highlight the interaction-dependent interfacial charge-transfer behavior based on both experimental observations and theoretical calculations. Experimental evidence points to charge transfer at the CdS–RGO interface playing a dominant role in the photocatalytic hydrogen production activity. By tuning the degree of reduction of RGO, the interfacial interaction, and, thereby, the charge transfer can be controlled at the CdS–RGO interface. This observation is supported by theoretical analysis, where we find that the interfacial charge transfer is a balance between the effective single-electron- and hole-transfer probability and the surface free electron and hole concentration, both of which are related to the surface potential and tailored by interfacial interaction. This mechanism is applicable to all systems for solar water splitting, providing a useful guidance for the design and study of heterointerfaces for high-efficiency energy conversion.

KEYWORDS: Solar water splitting, hydrogen fuel, graphene, interfacial interaction, interfacial charge transfer, dual-band-gap systems



Hydrogen generation from solar water splitting over semiconductor photocatalysts offers a promising solution to mitigate global energy crisis and reduce greenhouse gas emission because hydrogen can be stored, transported, and used without producing harmful byproducts.^{1–5} However, most solar water-splitting systems reported always have low efficiencies, mainly due to the high recombination rate of photogenerated electrons and holes.^{6,7} Recent computational investigations have further demonstrated that in rutile TiO₂ single-band-gap configuration, rather than its intrinsic catalytic activity, the low concentration of photogenerated holes reaching the surface is the main obstacle to oxygen evolution before it reaches the estimated threshold in the photocatalytic system.⁸ In comparison with single-band-gap systems, dual-band-gap systems can suppress charge recombination in the semiconductor because the built-in electric field formed at the interfacial region of two semiconductors, due to the equilibration of the individual Fermi levels, allows for charge separation, offers additional photovoltage to drive the surface reaction besides that produced at the semiconductor-liquid interface,^{9,10} and also serves to suppress the photocorrosion of semiconductors by efficient charge extraction.^{11–13} In addition,

dual-band-gap systems with an ideal theoretical efficiency of 41% have the best chance of realizing the minimum efficiency requirement of 10% for practical solar water splitting compared to single-band-gap systems.^{9,14} Thus, extensive efforts have been directed toward the development of different types of dual-band-gap systems, such as type I, type II, and Z schemes.^{15–21} In a type I band alignment for example, both conduction band (CB) and valence band (VB) edges of one semiconductor are localized within the energy gap of the other semiconductor, due to which an efficient separation of photogenerated charge carriers can occur, resulting in increased lifetime of photocarriers at the interface. This effect is due either to the difference between the migration rates of electrons and holes or to the passivation of surface states, typically in the CdS/ZnS photocatalyst, although both photogenerated electrons and holes transfer to the same semiconductor.^{18,20}

Received: November 28, 2018

Revised: December 31, 2018

Published: January 25, 2019

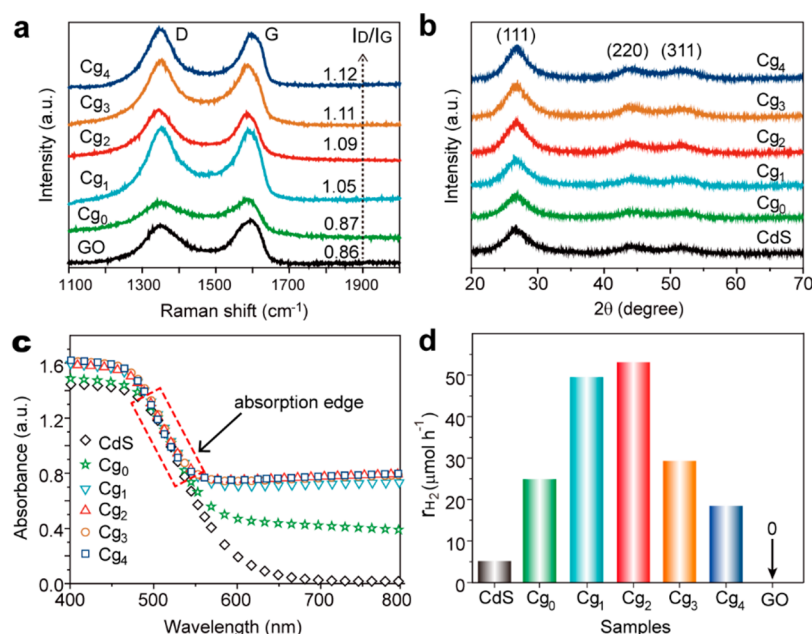


Figure 1. (a) Raman spectra of GO and CdS/RGO composites. (b) XRD patterns and (c) UV-vis diffuse reflectance spectra of CdS and CdS/RGO composites. (d) Visible-light driven photocatalytic H_2 production rate (r_{H_2}) of CdS, GO, and CdS/RGO composites. A 0.1 M Na_2S and 0.1 M Na_2SO_3 solution was used as the sacrificial reagent; a 350 W xenon arc lamp with a 420 nm cutoff filter was used as the light source.

In single-band-gap configuration, the kinetic charge transfer (CT) at the semiconductor/electrolyte interface depends both on the number of electrons/holes at the semiconductor surface and on the energetics of the semiconductor band edges.^{9,22,23} In dual-band-gap systems, the built-in electric field at the interface region of two semiconductors, which is characterized by surface potential in the semiconductors, has critical influence on interfacial CT behavior and, thereby, the solar water splitting activity as shown by experimental results.^{17,24,25} However, an in-depth physical mechanism explanation at the microscopic level applicable to all systems for solar water splitting has been missing so far,^{12,15,23,25} which is central to understanding and controlling the key process for efficient solar water splitting.

In this work, we have identified the critical role of interfacial charge transfer and attempted at a physical understanding of charge-transfer behavior modulated by interfacial interaction in a semiconductor CdS/reduced graphene oxide (RGO) composite model system for solar water splitting, using both experimental and theoretical approaches. We have chosen the CdS/RGO system as a case study for three reasons. First, dramatically improved photocatalytic performances have been experimentally observed over semiconductors based on graphene or graphene-derivatives such as RGO;^{26,27} second, the key role of the interface in facilitating charge separation when using CdS/RGO as a photocatalyst has been demonstrated, although no insight into the fundamental mechanism of this process has been provided;^{28,29} third, the electronic properties (especially the Fermi level) of RGO can be tuned in a wide range by controlling its degree of reduction, making RGO an ideal candidate material to investigate and control interfacial CT behavior.^{30–33} We have experimentally correlated the photocatalytic activity of CdS/RGO photocatalysts to the interfacial interaction-dependent CT behavior. In addition, our theoretical analysis reveals that interfacial charge transfer is a balance between the effective single-electron- and single-hole-transfer probability and the surface

free electron and hole concentration, both of which are associated with the surface potential and depend intimately on the interfacial interaction, thus providing support to our experimental observations. This mechanism can be generalized to all interfaces for solar water splitting and other energy conversion applications.

CdS/RGO nanocomposites with different degrees of reduction of RGO were synthesized by the solvothermal treatment of CdS/GO composites and labeled as Cg_0 , Cg_1 , Cg_2 , Cg_3 , and Cg_4 in the increasing order of the volume of hydrazine used in the reduction process (please see the [Experimental section of the Supporting Information](#) for more details). The stepwise reduction of RGO in the composites was verified by Raman and X-ray photoelectron spectroscopy (XPS) data. The Raman spectra of CdS/RGO composites in [Figure 1a](#) show the characteristic D and G bands of the carbon material,³⁴ and the intensity ratio of D to G band ($I_{\text{D}}/I_{\text{G}}$) can be used to evaluate RGO graphitization degree because the formation of new and small nanocrystalline sp^2 domains after removing oxygen-containing groups during the chemical reduction of GO can increase the $I_{\text{D}}/I_{\text{G}}$ ratio.^{35–38} The I_{D} -to- I_{G} ratios of CdS/RGO samples increase monotonically from 0.87 to 1.12 when going from Cg_0 to Cg_4 , indicating the gradual reduction of RGO in the composites. Moreover, the C-to-O ratio of RGO in the composites obtained from XPS spectra ([Figure S1](#)) increases from 4.63 for Cg_0 to 9.16 for Cg_4 due to the gradual removal of oxygen-containing groups in RGO sheets, which further proves that the degree of RGO reduction increases from Cg_0 to Cg_4 . XRD patterns ([Figure 1b](#)) indicate the formation of CdS with the cubic crystal structure (JCPDS no. 80-0019). From the width of the (111) diffraction peak and using the Scherrer formula, the average grain sizes of the CdS nanocrystals in the composites were estimated; these were found to be very similar ($\sim 2.2 \pm 0.2$ nm). Transmission electron microscopy (TEM) images show that the aggregated CdS nanocrystals form larger particles, most of which have sizes >50 nm, and no obvious change in

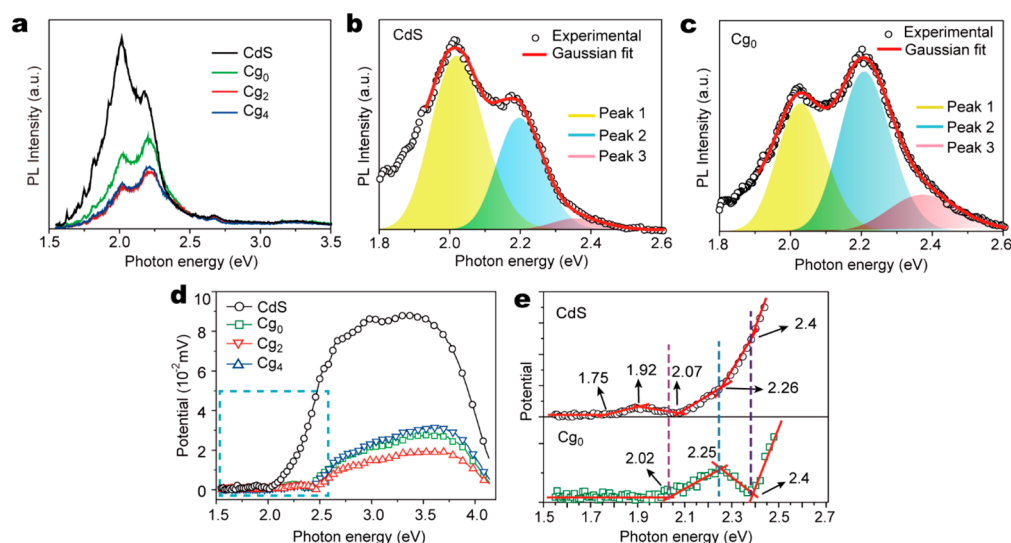


Figure 2. (a) PL spectra of CdS, Cg₀, Cg₂, and Cg₄. Gaussian fits to the PL spectra of (b) CdS and (c) Cg₀. (d) SPV spectra of CdS, Cg₀, Cg₂, and Cg₄. (e) Zoomed-in view on the blue rectangular section in panel d for isolated SPV spectra of CdS (top) and Cg₀ (bottom); regions of constant slope are fitted by straight lines, and the points of intersection of the lines are marked by arrows.

the morphology are observed in the CdS/RGO nanocomposites with different degrees of RGO reduction (Figure S2). The above results indicate that the reduction process has little effect on the crystal structure and morphology of CdS/RGO composites. To make sure that the prepared CdS/RGO composite is suitable for surface potential investigations, we have analyzed the band bending and band edges in CdS. For a 50 nm CdS particle, the potential drop between the surface and the center of the particle is calculated to be as high as 42 mV (see the [Band Bending in Photocatalysts](#) section in the [Supporting Information](#)). The high potential drop suggests that band bending occurs within the CdS particle and its contribution to the interfacial CT process cannot be neglected. Moreover, the flat-band potentials of the photocatalysts are not fixed by the possible adsorption of sulfide ions on the surface of CdS (Figure S3).³⁹ Thus, band bending and tunable band edges in CdS together render the CdS/RGO composite an ideal system to investigate the influence of the surface potential on the interfacial CT efficiency.

Following composition and structure characterization, the light absorption data of the composites were analyzed, from which four main conclusions can be drawn. (i) Little difference is seen in the optical absorption edges of the different composites (Figure 1c), displaying that their optical band gaps (i.e., absorption thresholds) are similar (Figure S4). This result indicates that optical absorption does not play a role in the difference in photocatalytic activity between the samples. (ii) The optical band gaps of all the composites (2.23–2.28 eV) are smaller than that of bulk CdS (2.42 eV), and Urbach tails are observed in the band gap for all of the samples, including bare CdS particles (Figures S5 and S6), which means that the observed band gap shrinking in CdS is presumably due to the presence of Urbach tails in the band gap.⁴⁰ (iii) CdS/RGO nanocomposites have larger Urbach energies than bare CdS particles (Figure S6). It is well-established that Urbach tails are caused by structural disorder and/or electron–phonon coupling (EPC). Therefore, it can be inferred that the presence of RGO might increase the degree of structural disorder in CdS, the EPC, or both.^{41–43} (iv) Finally, localized states associated with Urbach tails may act as shallow trap

states to prolong the lifetime of charge carriers and play a crucial role in CT behavior.^{44,45}

The solar water-splitting activity of the samples was accessed by measuring photocatalytic hydrogen production under visible-light irradiation (Figure 1d). Bare CdS has the lowest H₂ production rate of 5.21 μmol h^{−1}, which could be due to the rapid recombination of photoexcited electrons and holes.^{46–48} For the CdS/RGO composites, the degree of RGO reduction is found to have a significant influence on the activity of the CdS/RGO nanocomposites; the activity initially increases with increasing degree of RGO reduction, reaching the highest H₂ production rate of 53.06 μmol h^{−1} for Cg₂ and then decreases with further RGO reduction. The amount of H₂ evolved over each photocatalyst increases proportionally with reaction time (Figure S7), and no appreciable amount of H₂ is detected in the absence of either irradiation or photocatalyst in control experiments, suggesting that H₂ was produced exclusively by photocatalytic reactions on the photocatalysts. To explain the observed difference in photocatalytic activity among our samples, we first considered the effect of the variable proton reduction ability of the hydrazine-treated RGO. RGO with high reduction degree should possess a low proton reduction ability resulting from its lower number of oxygen containing groups.⁴⁹ Moreover, because no appreciable amount of H₂ is detected for bare GO and bare RGO with different reduction degrees under the same experimental conditions, this factor can be safely ruled out. Other possible influencing factors such as residual hydrazine, solubility of RGO, heating effect of RGO, and specific surface area have also been systematically excluded (see the [Other Factors that Possibly Influence Photocatalytic Activity](#) section, Figure S8, and Table S1 in the [Supporting Information](#)). Because both light absorption and surface proton reduction reaction appear to have little influence on the photocatalytic activity, we conclude that CT in the photocatalysts should instead play a dominant role.

To investigate the CT behavior in the nanocomposites, photoluminescence (PL) and surface photovoltage (SPV) spectroscopy were performed to obtain the energy distribution of localized states in the band gap of CdS.^{50–52} The four

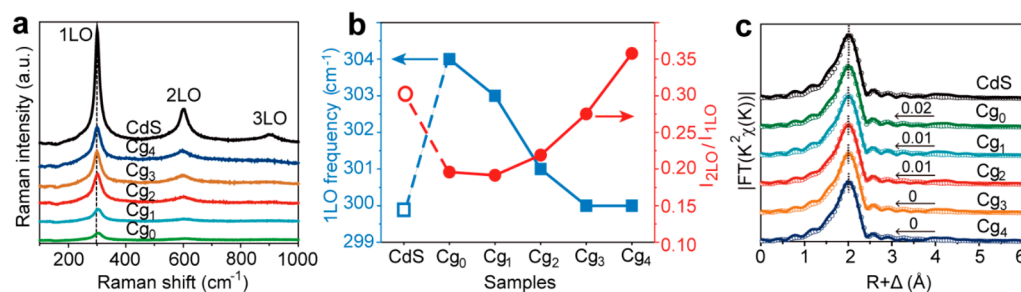


Figure 3. (a) Resonance Raman spectra of the samples taken in the range 100–1000 cm^{-1} . (b) Variation in the 1LO phonon frequency (blue) and $I_{2\text{LO}}/I_{1\text{LO}}$ value (red) for the different samples. (c) Fitting of Cd K-edge EXAFS spectra in the R space for bare CdS and CdS/RGO samples; solid lines are experimental data and hollow circles show fitting results. The number above each curve shows the left shifted value of the peak position (marked by the dashed line, corresponding to the Cd–S bond length) for CdS/RGO samples relative to that of bare CdS.

samples including bare CdS, Cg₀, Cg₂, and Cg₄ (all of which show typical photocatalytic activities) have a broad PL emission in the range of 1.5–3.0 eV (Figure 2a). The broad emission bands of bare CdS were fitted to three bands centered at 2.0 (peak 1), 2.2 (peak 2), and 2.4 eV (peak 3); some emission bands below 2.0 eV associated with deep trap states (unfitted) are also observed (Figure 2b).⁵³ The intense peak 1 is ascribed to the recombination of holes in the VB tail and electrons in deep trap states generated by sulfur vacancies (V_{S}^{2+}) in the CdS nanocrystals (Table S2).^{54,55} Taking into account the optical band gap of ~ 2.2 eV, peak 2 is assigned to recombination of electrons and holes at the CB tail and the VB tail. The weak peak 3 is attributed to the recombination of electrons trapped at shallow states due to cadmium interstitials and holes in the VB tail.⁵³ The high-intensity peak 1 dominates the PL spectrum of the bare CdS, suggesting a high rate of electron–hole recombination in deep trap states. The same three emission bands are also observed in the fitted PL spectra of the CdS/RGO composites (Figure 2c), where, compared to those of bare CdS, peaks 1 and 2 become much weaker, while peak 3 remains almost unaltered (Figure S9). This indicates that RGO can passivate deep trap states in CdS nanocrystals, thus promoting the quenching of PL emission originating from deep trap states but without affecting the CT pathways associated with shallow trap states. It is well-known that electrons trapped in deep trap states are energetically unfavorable for proton reduction; this passivation role of RGO is thus beneficial for hydrogen production because it makes more electrons and holes available for photocatalytic reactions. It is also seen that the intensity of PL initially decreases at low degree of RGO reduction (Cg₀ and Cg₂) but shows an increase when RGO in the nanocomposite is highly reduced (Cg₄) (Figure S9). This result indicates that for the CdS/RGO nanocomposites with high degree of RGO reduction, the CT from CdS to RGO is somewhat hampered, as compared to those with low degree of RGO reduction. Thus, CT from CdS to RGO is found to be closely associated with the degree of RGO reduction. This result is further confirmed from SPV spectral data. The SPV values of the CdS/RGO composites are much smaller than that of the bare CdS (Figure 2d), owing to the trapping of photoexcited electrons in CdS by RGO.⁵⁶ SPV data also show the highest charge separation efficiency of photoexcited carriers in Cg₂ due to its lowest SPV intensity. Additionally, as shown in Figure 2e, carrier transitions related to the V_{S}^{2+} -induced surface trap states (2.02–2.07 eV), band tail edges (2.25–2.26 eV), and shallow trap states (2.4 eV) are present in the SPV spectra of CdS and Cg₀, in agreement with PL results.⁵⁷ The two distinct

states appearing below 2.0 eV originating from deep trap states in the SPV spectrum of CdS are not detected for Cg₀, which validates the role of RGO in passivating deep trap states in CdS. Thus, our PL and SPV results clearly show that CT between CdS and RGO is first facilitated and then hindered with increasing degree of RGO reduction, and it corresponds well with observed dependence of photocatalytic activity on RGO reduction degree, confirming that interfacial CT between CdS and rGO is key to improving the photocatalytic activity of CdS/RGO composites.

It is known that interfacial CT behavior is closely related to the interaction of the two components at the interface,^{15,58} which, in our model system, are CdS and RGO. To reveal how the interaction between CdS and RGO varies with the degree of RGO reduction, resonance Raman spectroscopy was used to analyze the local strain at the interface.^{59–61} A pair of major bands assigned to the first- and the second-order longitudinal optical (1LO and 2LO) phonons in CdS are seen in the Raman spectra (Figure 3a).⁴⁰ The 1LO phonon peak of Cg₀ shifts to higher frequency by 4 cm^{-1} with respect to that in bare CdS (blue line in Figure 3b), indicating the presence of strain.^{59,62} The observed strain might be due to the presence of a large number of oxygen-containing groups on RGO in Cg₀ that allows for increased electrostatic interaction between RGO and CdS nanocrystals (Figure S10). This strong binding interaction can give rise to compressive strain in the CdS lattice. The presence of strain can be further confirmed by testing the local coordination environment of cadmium in the CdS/RGO composites via extended X-ray absorption fine structure (EXAFS) spectroscopy. EXAFS fitting results (Figure 3c and Table S3) show that the Cd–S bond length in Cg₀ is slightly lower than that in bare CdS, indicating the presence of compressive strain in CdS.^{63,64} Further reducing RGO will decrease the number of oxygen-containing groups, which in turn, reduces the electrostatic interaction between CdS and RGO, as a result of which the compressive strain is relaxed and the Cd–S bond length in CdS/RGO gradually recovers to its value in bare CdS; hence, the 1LO phonon peak in the Raman spectra shifts to lower frequency from Cg₀ to Cg₄. In addition, the increase in the Cd–S bond length leads to an increased relative ion displacement, which, in turn, will increase EPC in CdS.⁶⁵ This variation of EPC strength in CdS can be estimated by measuring the intensity ratio of the 2LO to 1LO ($I_{2\text{LO}}/I_{1\text{LO}}$) peaks in Raman spectra as a function of the degree of RGO reduction; it is seen that the intensity ratio increases with increasing degree of RGO reduction (red line in Figure 3b). Thus, changes in both the local strain and EPC confirm that

the interaction between CdS and RGO decreases with increasing degree of RGO reduction.

To unveil the relationship between CT and interaction at interfaces, we carried out theoretical calculations of the CdS/RGO system based on density functional theory (DFT).^{66,67} Our methodology involves the construction of five typical CdS/RGO models with decreasing number of hydroxyl groups in the RGO sheet, to represent the gradual increase in the degree of reduction of RGO, by systematically varying the interfacial interaction between CdS and RGO; these samples are denoted as CG₀, CG₁, CG₂, CG₃, and CG₄. The optimized structures of the five models are shown in Figure S11. The calculated binding energy between the CdS cluster and RGO sheet decreases with decreasing number of oxygen-containing groups (Table 1), indicating that the interaction between CdS

Table 1. Results of DFT Calculations for the Model System CdS/RGO

sample	E_b (eV) ^a	$d_{\text{Cd-S}}$ (Å) ^b	$\Delta\rho_z$ (10^{-3} e Å^{-3}) ^c
CdS	—	2.584	—
CG ₀	−8.14	2.548	+0.891
CG ₁	−7.68	2.550	+0.787
CG ₂	−1.25	2.567	−0.201
CG ₃	−1.14	2.579	−0.240
CG ₄	−0.28	2.579	−0.294

^a E_b is the binding energy. ^b $d_{\text{Cd-S}}$ is the average Cd–S bond length. ^c $\Delta\rho_z$ is the average interface charge density difference along the Z direction induced by interaction at the interface.

and RGO becomes weaker with increasing RGO reduction, which agrees well with the result from Raman spectra. The increase in the average length of the Cd–S bond with increasing RGO reduction degree is also consistent with the Cd–S bond length variation obtained from the EXAFS. To investigate the effect of the interfacial interaction on the CT between RGO and CdS, the planar-averaged charge density differences along the Z direction perpendicular to the RGO sheet were calculated for all the models. A dipole-like charge density distribution (pink region in Figure 4a) arises from the charge redistribution caused by the difference in Fermi levels between RGO and CdS, which leads to an interfacial dipole–dipole interaction.⁶⁸ These local interfacial dipoles give rise to a net electric field and modify the CdS surface potential V_s relative to its bulk Fermi level. Because the local interfacial charge density (ρ) increases monotonically with V_s , the change in V_s can be directly determined from a change in ρ ($\Delta\rho$). The average $\Delta\rho$ values along the Z direction ($\Delta\rho_z$) induced by interfacial interaction for the different CdS/RGO samples are listed in Table 1. A negative shift in $\Delta\rho_z$ at the interface is seen when the interfacial interaction becomes weaker due to increased reduction of RGO; this will lead to a decrease in the local interfacial charge density as well as in the surface potential V_s on CdS.

At thermal equilibrium, the free electron concentration on the surface of CdS in the CdS/RGO system in the dark is:⁶⁹

$$n_s = n_0 e^{-qV_s/k_B T} \quad (1)$$

where n_0 is the thermal equilibrium free electron concentration in the bulk of the semiconductor, k_B is the Boltzmann constant, T is the absolute temperature in Kelvin, and q is the charge of electron. Eq 1 suggests that the free electron concentration on the surface of CdS is higher at lower V_s values. Based on

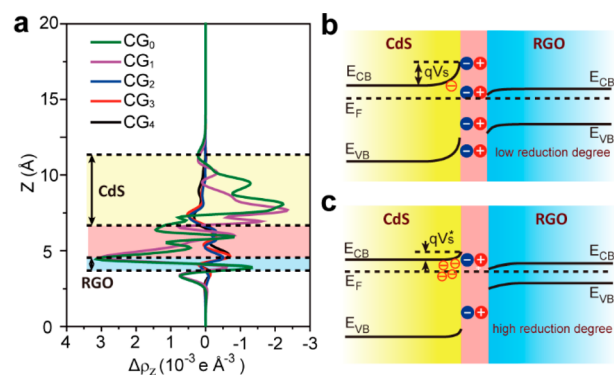


Figure 4. (a) Planar-averaged electron density difference $\Delta\rho_z$ along the Z direction for the five model composites. Diagrams of interfacial potential and charge distribution for the CdS/RGO system (b) with low RGO reduction degree and (c) with high RGO reduction degree. E_{CB} , E_{VB} , and E_{F} are the conduction band minimum, valence band maximum, and Fermi level, respectively. The pink zone represents the interface between CdS and RGO and blue and red circles with plus and minus signs denote local interfacial electrons and holes respectively; surface free electrons on CdS are shown by orange open circles. Systems with higher RGO reduction degree are found to have weaker interaction, less local interfacial charge density, smaller V_s , and higher surface free electron concentration n_s .

previous studies on the band structure of CdS and RGO,^{70–72} a Type I band alignment between CdS and RGO can be confirmed regardless of the reduction degree of RGO in our systems. Accordingly, the surface potential and charge distribution for the RGO/CdS system with low and high reduction degree of RGO are illustrated in Figure 4b,c.

Based on Marcus theory^{73,74} and assuming pinning of the Fermi level of the RGO surface at a certain value owing to its high density of states, the interfacial electron-transfer rate can be written as:

$$k_{\text{ET}} = n_s(qV_s)k_{0,n}(H_{\text{DA}}, \lambda, qV_s) \quad (2)$$

where $k_{0,n}$ can be understood as an effective single-electron-transfer probability, which increases as the driving force qV_s increases. From eq 2, it is clear that the total electron-transfer rate is the product of the surface free electron concentration and the effective single-electron-transfer probability. Considering both electron and hole transfer at the interface, the interfacial CT photocurrent density is written as (the detail can be found in the Interfacial Charge Transfer section of the Supporting Information)

$$j_{\text{int}}^{\text{light}} \approx q(n_s^{\text{light}} - n_s)k_{0,n} - q(p_s^{\text{light}} - p_s)k_{0,p} \quad (3)$$

where n_s^{light} is the surface free electron concentration under irradiation; p_s^{light} and p_s are the surface free hole concentrations under irradiation and in the dark, respectively; and $k_{0,p}$ is the effective single-hole-transfer probability. The expression for $j_{\text{int}}^{\text{light}}$ suggests that two factors determine the steady photocurrent of a photocatalyst, namely, the surface free electron/hole concentration and the effective single electron- and hole-transfer probability. Here, it should be noted that as the surface free electron and hole concentration and the effective single electron- and hole-transfer probability are associated with the surface potential, the above model will be invalid if band bending at the interface is no longer effective as in the case of quantum dots.⁷⁵ Because the electron and hole currents show similar behavior except for moving in opposite directions, we

consider only the case of the electron current in the following discussion. When the surface potential V_s on CdS is decreased, the free electron concentration n_s on the surface of CdS increases, while the effective single-electron-transfer probability $k_{0,n}$ decreases. As a result, the maximum interfacial photocurrent density can be expected at some intermediate value of V_s , where the product of the free electron concentration on the surface and the effective single-electron-transfer probability is a maximum. Because V_s decreases with increasing degree of reduction of RGO in the composites, it is obvious that the interfacial photocurrent density, i.e., the photocatalytic activity, can be maximized by controlling the degree of reduction of RGO at an intermediate value.

Based on the above experimental and theoretical analysis, the underlying mechanism for the photocatalytic activity of CdS/RGO can be understood as follows: in bare CdS, most photoexcited electrons are captured by deep traps and recombine with photoexcited holes, leading to a low photocatalytic activity. Upon introducing RGO, deep traps present in CdS are passivated, which increases surface free electron concentration n_s , resulting in a greater number of electrons and holes to transfer from CdS to RGO through the conduction band and the valence band of CdS, respectively. Owing to the upward band bending on the CdS surface, the transfer of holes to RGO is easier than the transfer of electrons due to the absence of energy barrier for holes. The hole has a higher mobility than electron in RGO⁷⁶ and can therefore be quickly consumed by the $\text{Na}_2\text{S}/\text{Na}_2\text{SO}_3$ hole scavengers, thus ensuring that electrons react with protons for efficient hydrogen evolution on RGO. Here, it should be emphasized that the feasibility of this process is closely related to degree of reduction of RGO. With increasing RGO reduction degree, the interfacial interaction between CdS and RGO is weakened, which decreases the surface potential V_s on CdS, simultaneously leading to a monotonic increase in surface free electron concentration n_s but a corresponding decrease in single-electron-transfer probability $k_{0,n}$. Consequently, the photocatalytic activity of CdS/RGO photocatalysts reaches its highest level at some intermediate degree of RGO reduction, which, in our case, corresponds to the sample Cg₂.

In conclusion, using a combination of theory and experiment, we have attempted to gain insightful understanding on the interfacial interaction-dependent charge-transfer behavior using CdS/RGO nanocomposites as a model system. Owing to a modulation of the interfacial charge transfer by variations in CdS–RGO interactions, the photocatalytic activity of CdS/RGO photocatalysts shows a non-monotonic behavior with an increasing degree of RGO reduction; this trend results from a decrease in effective single-electron-transfer probability and an increase in surface free electron concentration. The above results show that it is the interfacial charge transfer rather than the intrinsic catalytic activity of the photocatalyst that plays a dominant role to determine the photocatalytic activity in the CdS/RGO system, and the charge-transfer behavior can, in turn, be finely controlled by tailoring interfacial interaction. These findings can be generalized to photoelectrochemical water-splitting processes, where the surface potential as well as the interfacial state coupling could be affected by the applied external electric field and both the effective single electron- and hole-transfer probability and the surface free electron and hole concentration will be changed accordingly, and also to other solar energy conversion systems after a modification of specific parameters for the system under study. Thus, our work

provides useful guidance for the design and study of heterointerfaces for high-efficiency energy conversion.

■ ASSOCIATED CONTENT

§ Supporting Information

The Supporting Information is available free of charge on the ACS Publications website at DOI: 10.1021/acs.nanolett.8b04768.

Details on the experimental methods, computational calculations, sample characterization, XPS survey spectra, hydrogen generation, models and computations, band bending, residual hydrazine, solubility of RGO, specific surface areas, heating effects of RGO, and interfacial charge transfer; figures showing XPS spectra, TEM images, Mott–Schottky plots, determination of band gaps, variation of absorption coefficients, time courses, FTIR spectroscopy, PL intensities, views of optimized geometries, and an experimental schematic; and tables showing specific surface areas, elemental composition, and parameters of local structure (PDF)

■ AUTHOR INFORMATION

Corresponding Author

*E-mail: gongjr@nanoctr.cn.

ORCID

Jian Ru Gong: 0000-0003-1512-4762

Author Contributions

[†]G.X., L.G., and L.Z. contributed equally.

Notes

The authors declare no competing financial interest.

■ ACKNOWLEDGMENTS

The authors acknowledge financial support for this work from the National Natural Science Foundation of China (grant nos. 21422303, 21573049, 21872043, and 81602643), the National Key R&D Program “nanotechnology” special focus (grant no. 2016YFA0201600), the Beijing Natural Science Foundation (2142036), and the Knowledge Innovation Program, Youth Innovation Promotion Association, and Special Program of “One Belt One Road” of CAS. We thank Prof. Dejun Wang and Prof. Tengfeng Xie from Jilin University for their help with the SPV setup. We also thank Dr. Kai Zhang for his helpful discussions.

■ REFERENCES

- (1) Pham, T. A.; Ping, Y.; Galli, G. Modelling Heterogeneous Interfaces for Solar Water Splitting. *Nat. Mater.* **2017**, *16*, 401–408.
- (2) Chen, X.; Shen, S.; Guo, L.; Mao, S. S. Semiconductor-based Photocatalytic Hydrogen Generation. *Chem. Rev.* **2010**, *110* (11), 6503–6570.
- (3) Maeda, K.; Teramura, K.; Lu, D.; Takata, T.; Saito, N.; Inoue, Y.; Domen, K. Photocatalyst Releasing Hydrogen from Water. *Nature* **2006**, *440* (7082), 295–295.
- (4) Chen, S.; Takata, T.; Domen, K. Particulate Photocatalysts for Overall Water Splitting. *Nat. Rev. Mater.* **2017**, *2* (10), 17050.
- (5) Guo, B.; Tian, L.; Xie, W.; Batool, A.; Xie, G.; Xiang, Q.; Jan, S. U.; Boddula, R.; Gong, J. R. Vertically Aligned Porous Organic Semiconductor Nanorod Array Photoanodes for Efficient Charge Utilization. *Nano Lett.* **2018**, *18* (9), 5954–5960.
- (6) Dotan, H.; Sivula, K.; Grätzel, M.; Rothschild, A.; Warren, S. C. Probing the photoelectrochemical properties of hematite ($\alpha\text{-Fe}_2\text{O}_3$) electrodes using hydrogen peroxide as a hole scavenger. *Energy Environ. Sci.* **2011**, *4* (3), 958–964.

- (7) Kesselman, J. M.; Shreve, G. A.; Hoffmann, M. R.; Lewis, N. S. Flux-matching conditions at TiO₂ photoelectrodes: is interfacial electron transfer to O₂ rate-limiting in the TiO₂-catalyzed photochemical degradation of organics? *J. Phys. Chem.* **1994**, *98* (50), 13385–13395.
- (8) Wang, D.; Sheng, T.; Chen, J.; Wang, H.-F.; Hu, P. Identifying the key obstacle in photocatalytic oxygen evolution on rutile TiO₂. *Nat. Catal.* **2018**, *1* (4), 291–299.
- (9) Walter, M. G.; Warren, E. L.; McKone, J. R.; Boettcher, S. W.; Mi, Q.; Santori, E. A.; Lewis, N. S. Solar water splitting cells. *Chem. Rev.* **2010**, *110* (11), 6446–6473.
- (10) Mayer, M. T.; Lin, Y.; Yuan, G.; Wang, D. Forming heterojunctions at the nanoscale for improved photoelectrochemical water splitting by semiconductor materials: case studies on hematite. *Acc. Chem. Res.* **2013**, *46* (7), 1558–1566.
- (11) Zhang, J.; Guo, Y.; Xiong, Y.; Zhou, D.; Dong, S. An environmentally friendly Z-scheme WO₃/CDots/CdS heterostructure with remarkable photocatalytic activity and anti-photocorrosion performance. *J. Catal.* **2017**, *356*, 1–13.
- (12) Qin, Z.; Xue, F.; Chen, Y.; Shen, S.; Guo, L. Spatial charge separation of one-dimensional Ni₂P-Cd_{0.9}Zn_{0.1}S/g-C₃N₄ heterostructure for high-quantum-yield photocatalytic hydrogen production. *Appl. Catal., B* **2017**, *217*, 551–559.
- (13) Aguirre, M. E.; Zhou, R.; Eugene, A. J.; Guzman, M. I.; Grela, M. A. Cu₂O/TiO₂ heterostructures for CO₂ reduction through a direct Z-scheme: Protecting Cu₂O from photocorrosion. *Appl. Catal., B* **2017**, *217*, 485–493.
- (14) Bolton, J. R.; Strickler, S. J.; Connolly, J. S. Limiting and realizable efficiencies of solar photolysis of water. *Nature* **1985**, *316*, 495.
- (15) Ye, M. Y.; Zhao, Z. H.; Hu, Z. F.; Liu, L. Q.; Ji, H. M.; Shen, Z. R.; Ma, T. Y. 0D/2D Heterojunctions of Vanadate Quantum Dots/Graphitic Carbon Nitride Nanosheets for Enhanced Visible-Light-Driven Photocatalysis. *Angew. Chem., Int. Ed.* **2017**, *56* (29), 8407–8411.
- (16) Cho, Y.; Kim, S.; Park, B.; Lee, C.-L.; Kim, J. K.; Lee, K.-S.; Choi, I. Y.; Kim, J. K.; Zhang, K.; Oh, S. H.; Park, J. H. Multiple Heterojunction in Single Titanium Dioxide Nanoparticles for Novel Metal-Free Photocatalysis. *Nano Lett.* **2018**, *18* (7), 4257–4262.
- (17) Wang, H.; Zhang, L.; Chen, Z.; Hu, J.; Li, S.; Wang, Z.; Liu, J.; Wang, X. Semiconductor Heterojunction Photocatalysts: Design, Construction, and Photocatalytic Performances. *Chem. Soc. Rev.* **2014**, *43* (15), S234–S244.
- (18) Li, H.; Zhou, Y.; Tu, W.; Ye, J.; Zou, Z. State-of-the-Art Progress in Diverse Heterostructured Photocatalysts toward Promoting Photocatalytic Performance. *Adv. Funct. Mater.* **2015**, *25* (7), 998–1013.
- (19) Yang, J.; Wang, D.; Han, H.; Li, C. Roles of cocatalysts in photocatalysis and photoelectrocatalysis. *Acc. Chem. Res.* **2013**, *46* (8), 1900–1909.
- (20) Huang, L.; Wang, X.; Yang, J.; Liu, G.; Han, J.; Li, C. Dual cocatalysts loaded type I CdS/ZnS core/shell nanocrystals as effective and stable photocatalysts for H₂ evolution. *J. Phys. Chem. C* **2013**, *117* (22), 11584–11591.
- (21) Fang, Z.; Liu, Y.; Fan, Y.; Ni, Y.; Wei, X.; Tang, K.; Shen, J.; Chen, Y. Epitaxial growth of CdS nanoparticle on Bi₂S₃ nanowire and photocatalytic application of the heterostructure. *J. Phys. Chem. C* **2011**, *115* (29), 13968–13976.
- (22) Kamat, P. V. Manipulation of Charge Transfer across Semiconductor Interface. A Criterion That Cannot Be Ignored in Photocatalyst Design. *J. Phys. Chem. Lett.* **2012**, *3* (5), 663–672.
- (23) Xu, Q.; Zhu, B.; Jiang, C.; Cheng, B.; Yu, J. Constructing 2D/2D Fe₂O₃/g-C₃N₄ Direct Z-Scheme Photocatalysts with Enhanced H₂ Generation Performance. *Solar RRL* **2018**, *2* (3), 1800006.
- (24) Park, H.; Kim, H.-i.; Moon, G.-h.; Choi, W. Photoinduced Charge Transfer Processes in Solar Photocatalysis Based on Modified TiO₂. *Energy Environ. Sci.* **2016**, *9* (2), 411–433.
- (25) Qiu, B.; Zhu, Q.; Du, M.; Fan, L.; Xing, M.; Zhang, J. Efficient Solar Light Harvesting CdS/Co₉S₈ Hollow Cubes for Z-Scheme Photocatalytic Water Splitting. *Angew. Chem.* **2017**, *129* (10), 2728–2732.
- (26) Xie, G.; Zhang, K.; Guo, B.; Liu, Q.; Fang, L.; Gong, J. R. Graphene-Based Materials for Hydrogen Generation from Light-Driven Water Splitting. *Adv. Mater.* **2013**, *25* (28), 3820–3839.
- (27) Li, Q.; Guo, B.; Yu, J.; Ran, J.; Zhang, B.; Yan, H.; Gong, J. R. Highly Efficient Visible-light-driven Photocatalytic Hydrogen Production of CdS-cluster-decorated Graphene Nanosheets. *J. Am. Chem. Soc.* **2011**, *133* (28), 10878–10884.
- (28) Li, Q.; Li, X.; Wageh, S.; Al-Ghamdi, A. A.; Yu, J. CdS/graphene nanocomposite photocatalysts. *Adv. Energy Mater.* **2015**, *5* (14), 1500010.
- (29) Jia, L.; Wang, D.-H.; Huang, Y.-X.; Xu, A.-W.; Yu, H.-Q. Highly durable N-doped graphene/CdS nanocomposites with enhanced photocatalytic hydrogen evolution from water under visible light irradiation. *J. Phys. Chem. C* **2011**, *115* (23), 11466–11473.
- (30) Mathkar, A.; Tozier, D.; Cox, P.; Ong, P.; Galande, C.; Balakrishnan, K.; Leela Mohana Reddy, A.; Ajayan, P. M. Controlled, Stepwise Reduction and Band Gap Manipulation of Graphene Oxide. *J. Phys. Chem. Lett.* **2012**, *3* (8), 986–991.
- (31) Yan, J.-A.; Xian, L.; Chou, M. Structural and Electronic Properties of Oxidized Graphene. *Phys. Rev. Lett.* **2009**, *103* (8), No. 086802.
- (32) Eda, G.; Mattevi, C.; Yamaguchi, H.; Kim, H.; Chhowalla, M. Insulator to Semimetal Transition in Graphene Oxide. *J. Phys. Chem. C* **2009**, *113* (35), 15768–15771.
- (33) Zhang, J.; Yu, J.; Jaroniec, M.; Gong, J. R. Noble Metal-free Reduced Graphene Oxide-Zn_xCd_{1-x}S Nanocomposite with Enhanced Solar Photocatalytic H₂-production Performance. *Nano Lett.* **2012**, *12* (9), 4584–4589.
- (34) Ferrari, A. C.; Robertson, J. Resonant Raman Spectroscopy of Disordered, Amorphous, and Diamondlike Carbon. *Phys. Rev. B: Condens. Matter Mater. Phys.* **2001**, *64* (7), No. 075414.
- (35) He, H.; Luo, F.; Qian, N.; Wang, N. Improved Microwave Absorption and Electromagnetic Properties of BaFe₁₂O₁₉-poly(vinylidene fluoride) Composites by Incorporating Reduced Graphene Oxides. *J. Appl. Phys.* **2015**, *117* (8), No. 085502.
- (36) Shen, Y.; Yang, S.; Zhou, P.; Sun, Q.; Wang, P.; Wan, L.; Li, J.; Chen, L.; Wang, X.; Ding, S.; et al. Evolution of the Band-gap and Optical Properties of Graphene Oxide with Controllable Reduction Level. *Carbon* **2013**, *62*, 157–164.
- (37) Stankovich, S.; Dikin, D. A.; Piner, R. D.; Kohlhaas, K. A.; Kleinhammes, A.; Jia, Y.; Wu, Y.; Nguyen, S. T.; Ruoff, R. S. Synthesis of Graphene-based Nanosheets via Chemical Reduction of Exfoliated Graphite Oxide. *Carbon* **2007**, *45* (7), 1558–1565.
- (38) Conway, N. M. J.; Ferrari, A. C.; Flewitt, A. J.; Robertson, J.; Milne, W. I.; Tagliaferro, A.; Beyer, W. Defect and Disorder Reduction by Annealing in Hydrogenated Tetrahedral Amorphous Carbon. *Diamond Relat. Mater.* **2000**, *9* (3–6), 765–770.
- (39) Frame, F. A.; Osterloh, F. E. CdSe-MoS₂: a quantum size-confined photocatalyst for hydrogen evolution from water under visible light. *J. Phys. Chem. C* **2010**, *114* (23), 10628–10633.
- (40) Chandramohan, S.; Kanjilal, A.; Sarangi, S. N.; Majumder, S.; Sathyamoorthy, R.; Som, T. Implantation-assisted Co-doped CdS Thin Films: Structural, Optical, and Vibrational Properties. *J. Appl. Phys.* **2009**, *106* (6), No. 063506.
- (41) El-Diasty, F.; Abdel Wahab, F. A.; Abdel-Baki, M. Optical Band Gap Studies on Lithium Aluminum Silicate Glasses Doped with Cr³⁺ ions. *J. Appl. Phys.* **2006**, *100* (9), No. 093511.
- (42) Moustafa, M.; Zandt, T.; Janowitz, C.; Mancke, R. Growth and Band Gap Determination of the Zr₃Se_{2-x} Single Crystal Series. *Phys. Rev. B: Condens. Matter Mater. Phys.* **2009**, *80* (3), No. 035206.
- (43) Tang, H.; Levy, F.; Berger, H.; Schmid, P. E. Urbach tail of Anatase TiO₂. *Phys. Rev. B: Condens. Matter Mater. Phys.* **1995**, *52* (11), 7771.
- (44) Kong, M.; Li, Y.; Chen, X.; Tian, T.; Fang, P.; Zheng, F.; Zhao, X. Tuning the Relative Concentration Ratio of Bulk Defects to Surface Defects in TiO₂ Nanocrystals Leads to High Photocatalytic Efficiency. *J. Am. Chem. Soc.* **2011**, *133* (41), 16414–16417.

- (45) Hao, E.; Anderson, N. A.; Asbury, J. B.; Lian, T. Effect of Trap States on Interfacial Electron Transfer Between Molecular Absorbates and Semiconductor Nanoparticles. *J. Phys. Chem. B* **2002**, *106* (39), 10191–10198.
- (46) Utterback, J. K.; Grennell, A. N.; Wilker, M. B.; Pearce, O. M.; Eaves, J. D.; Dukovic, G. Observation of Trapped-hole Diffusion on the Surfaces of CdS Nanorods. *Nat. Chem.* **2016**, *8* (11), 1061–1066.
- (47) Klimov, V.; Bolivar, P. H.; Kurz, H. Ultrafast Carrier Dynamics in Semiconductor Quantum Dots. *Phys. Rev. B: Condens. Matter Mater. Phys.* **1996**, *53* (3), 1463–1467.
- (48) Zhang, J.; Qiao, S. Z.; Qi, L.; Yu, J. Fabrication of NiS Modified CdS Nanorod p-n Junction Photocatalysts with Enhanced Visible-light Photocatalytic H₂-production Activity. *Phys. Chem. Chem. Phys.* **2013**, *15* (29), 12088–12094.
- (49) Jiao, Y.; Zheng, Y.; Davey, K.; Qiao, S.-Z. Activity origin and catalyst design principles for electrocatalytic hydrogen evolution on heteroatom-doped graphene. *Nat. Energy* **2016**, *1* (10), 16130.
- (50) Knorr, F. J.; Mercado, C. C.; McHale, J. L. Trap-State Distributions and Carrier Transport in Pure and Mixed-Phase TiO₂: Influence of Contacting Solvent and Interphasial Electron Transfer. *J. Phys. Chem. C* **2008**, *112* (33), 12786–12794.
- (51) Kronik, L. Surface Photovoltage Phenomena: Theory, Experiment, and Applications. *Surf. Sci. Rep.* **1999**, *37* (1–5), 1–206.
- (52) Li, S.; Zhang, L.; Jiang, T.; Chen, L.; Lin, Y.; Wang, D.; Xie, T. Construction of Shallow Surface States through Light Ni Doping for High-Efficiency Photocatalytic Hydrogen Production of CdS Nanocrystals. *Chem. - Eur. J.* **2014**, *20* (1), 311–316.
- (53) Narayanam, P. K.; Soni, P.; Mohanta, P.; Srinivasa, R. S.; Talwar, S. S.; Major, S. S. Effect of Heat Treatment on the Photoluminescence of CdS Nanocrystallites in Cadmium-rich Organic Langmuir Blodgett Matrix. *Mater. Chem. Phys.* **2013**, *139* (1), 196–209.
- (54) Chandran, A.; Samuel, M. S.; Koshy, J.; George, K. C. Correlated Barrier Hopping in CdS Nanoparticles and Nanowires. *J. Appl. Phys.* **2011**, *109* (8), No. 084314.
- (55) Abken, A. E.; Halliday, D. P.; Durose, K. Photoluminescence Study of Polycrystalline Photovoltaic CdS Thin Film Layers Grown by Close-spaced Sublimation and Chemical Bath Deposition. *J. Appl. Phys.* **2009**, *105* (6), No. 064515.
- (56) Wang, J.; Zhao, J.; Osterloh, F. E. Photochemical Charge Transfer Observed in Nanoscale Hydrogen Evolving Photocatalysts Using Surface Photovoltage Spectroscopy. *Energy Environ. Sci.* **2015**, *8* (10), 2970–2976.
- (57) Burstein, L.; Shapira, Y.; Bennett, B. R.; del Alamo, J. A. Surface Photovoltage Spectroscopy of In_xAl_{1-x}As Epilayers. *J. Appl. Phys.* **1995**, *78* (12), 7163.
- (58) Long, R.; Fang, W.-H.; Prezhdov, O. V. Strong Interaction at the Perovskite/TiO₂ Interface Facilitates Ultrafast Photoinduced Charge Separation: A Nonadiabatic Molecular Dynamics Study. *J. Phys. Chem. C* **2017**, *121* (7), 3797–3806.
- (59) Zardo, I.; Conesa-Boj, S.; Peiro, F.; Morante, J.; Arbiol, J.; Uccelli, E.; Abstreiter, G.; Fontcuberta i Morral, A. Raman Spectroscopy of Wurtzite and Zinc-blende GaAs Nanowires: Polarization Dependence, Selection Rules, and Strain Effects. *Phys. Rev. B: Condens. Matter Mater. Phys.* **2009**, *80* (24), 245324.
- (60) Alivisatos, A.; Harris, T.; Carroll, P.; Steigerwald, M.; Brus, L. Electron-vibration Coupling in Semiconductor Clusters Studied by Resonance Raman Spectroscopy. *J. Chem. Phys.* **1989**, *90* (7), 3463–3468.
- (61) Hu, C.; Zeng, X.; Cui, J.; Chen, H.; Lu, J. Size Effects of Raman and Photoluminescence Spectra of CdS Nanobelts. *J. Phys. Chem. C* **2013**, *117* (40), 20998–21005.
- (62) Xu, C. Y.; Zhang, P. X.; Yan, L. Blue Shift of Raman Peak from Coated TiO₂ Nanoparticles. *J. Raman Spectrosc.* **2001**, *32* (10), 862–865.
- (63) Lu, P.; Wu, X.; Guo, W.; Zeng, X. C. Strain-dependent electronic and magnetic properties of MoS₂ monolayer, bilayer, nanoribbons and nanotubes. *Phys. Chem. Chem. Phys.* **2012**, *14* (37), 13035–13040.
- (64) Woicik, J. C.; Pellegrino, J. G.; Steiner, B.; Miyano, K. E.; Bompadre, S. G.; Sorensen, L. B.; Lee, T. L.; Khalid, S. Bond-Length Distortions in Strained Semiconductor Alloys. *Phys. Rev. Lett.* **1997**, *79* (25), 5026–5029.
- (65) Li, Z. *Solid State Theory*, 2nd ed.; Higher Education Press: Beijing, China, 2014.
- (66) Kresse, G.; Furthmüller, J. Efficiency of ab-initio Total Energy Calculations for Metals and Semiconductors Using a Plane-wave Basis Set. *Comput. Mater. Sci.* **1996**, *6* (1), 15–50.
- (67) Kresse, G.; Furthmüller, J. Efficient Iterative Schemes for ab initio Total-energy Calculations Using a Plane-wave Basis Set. *Phys. Rev. B: Condens. Matter Mater. Phys.* **1996**, *54* (16), 11169.
- (68) Cheng, K.; Han, N.; Su, Y.; Zhang, J.; Zhao, J. Schottky Barrier at Graphene/Metal Oxide Interfaces: Insight from First-principles Calculations. *Sci. Rep.* **2017**, *7*, 41771.
- (69) Mills, T. J.; Lin, F.; Boettcher, S. W. Theory and Simulations of Electrocatalyst-coated Semiconductor Electrodes for Solar Water Splitting. *Phys. Rev. Lett.* **2014**, *112* (14), 148304.
- (70) Yeh, T.-F.; Chan, F.-F.; Hsieh, C.-T.; Teng, H. Graphite oxide with different oxygenated levels for hydrogen and oxygen production from water under illumination: the band positions of graphite oxide. *J. Phys. Chem. C* **2011**, *115* (45), 22587–22597.
- (71) Yeh, T. F.; Syu, J. M.; Cheng, C.; Chang, T. H.; Teng, H. Graphite oxide as a photocatalyst for hydrogen production from water. *Adv. Funct. Mater.* **2010**, *20* (14), 2255–2262.
- (72) Kudo, A.; Miseki, Y. Heterogeneous photocatalyst materials for water splitting. *Chem. Soc. Rev.* **2009**, *38* (1), 253–278.
- (73) Zhu, H.; Yang, Y.; Wu, K.; Lian, T. Charge Transfer Dynamics from Photoexcited Semiconductor Quantum Dots. *Annu. Rev. Phys. Chem.* **2016**, *67*, 259–281.
- (74) Marcus, R. A. Chemical and Electrochemical Electron-Transfer Theory. *Annu. Rev. Phys. Chem.* **1964**, *15* (1), 155–196.
- (75) Hagfeldt, A.; Graetzel, M. Light-induced redox reactions in nanocrystalline systems. *Chem. Rev.* **1995**, *95* (1), 49–68.
- (76) Wang, S.; Ang, P. K.; Wang, Z.; Tang, A. L. L.; Thong, J. T.; Loh, K. P. High mobility, printable, and solution-processed graphene electronics. *Nano Lett.* **2010**, *10* (1), 92–98.